

Electrochemical Performance of Sandwich-like Structured TiO₂/graphene Composite as Anode for Potassium-ion Batteries

Wenna Li^{1,2}, Nengshuang Gao², Siqi Cheng², Jihua Wu^{1,*}, Quanqi Chen^{1,2,**}

¹ Intelligent Manufacturing Institute, Taizhou University, Taizhou 318000, China

² Guangxi Key Laboratory of Electrochemical and Magneto-chemical Functional Materials, College of Chemistry and Bioengineering, Guilin University of Technology, Guilin 541004, China

*E-mail: wujihua@tzc.edu.cn

**E-mail: quanqi.chen@glut.edu.cn

Received: 6 September 2022 / Accepted: 24 October 2022 / Published: 17 November 2022

The TiO₂/graphene composite was synthesized by a simple hydrothermal reaction combined with a post high-temperature sintering in an inert atmosphere using graphene oxide (GO), butyl titanate and NaOH as raw materials. The TiO₂/graphene composite is composed of mesoporous graphene nanosheets and dispersive TiO₂ nanoparticles that are attached to the surface and reside in the interlayer of graphene. Benefiting from the special microstructure and synergetic effects of electroactive materials TiO₂ and graphene, TiO₂/graphene composite is superior in charge capacity, rate capability and cycle performance to both graphene and TiO₂. As anode materials for potassium-ion batteries, TiO₂/graphene, graphene and TiO₂ present initial charge capacities of 336.8, 261.9 and 30.3 mAh g⁻¹ at 100 mA g⁻¹, respectively, and maintain 245, 135.5 and 18.5 mAh g⁻¹ after 100 cycles, respectively. Even at a high current density of 600 mA g⁻¹, the remaining charge capacity of TiO₂/graphene is 120 mAh g⁻¹ after 100 cycles, significantly higher than those of graphene (50.7 mAh g⁻¹) and TiO₂ (4.5 mAh g⁻¹).

Keywords: graphene; hydrothermal; potassium-ion batteries; sandwich; anode

1. INTRODUCTION

The potassium-ion battery (PIB) has recently been attractive for large-scale applications owing to the advantages such as plentiful potassium resources and lower standard electrode potential for K⁺/K [1]. The potassium (2.09 wt%) is greatly more plentiful than lithium (0.0017 wt%) in Earth's crust, making the cost of PIBs much lower than that of LIBs in nature. Moreover, the standard potential of the K⁺/K couple (-2.93 V vs. SHE) is lower than that of the Na⁺/Na couple (-2.71 V vs. SHE) and comparable to that of the Li⁺/Li couple (-3.04 V vs. SHE), which is favorable for PIBs to approach the high voltage and energy density of LIBs [2]. Nevertheless, K⁺ has larger radius than both Li⁺ and Na⁺, making it

difficult for K^+ to transport rapidly in the electroactive particles with the similar host structure to that of Li and Na analogs, resulting in the humble electrochemical performance. Thus, it is imperative to search for electrode materials, which accommodate the larger K^+ and provide the larger space for quick K^+ transfer.

As for anode materials, the explored materials are mainly categorized as nonmetallic elements [3-7], metals [8, 9], alloys [10, 11], chalcogenides [12-14] and their corresponding composites [15-18], and the carbon-based materials have been extensively investigated due to the great profusion of carbon resources in nature, relatively larger channel for k^+ transport, and the smaller volume expansion of the host upon charging, which is helpful for the improvement of cyclability of the electrode [4, 19-26]. Among the carbon-based materials, graphene has attracted enormous interests owing to its high specific surface area, abundance of active sites, and excellent mechanic properties and electron mobility. However, the pristine graphene anode [27, 28] exhibits much lower capacity than the theoretical capacity of 279 mAh g^{-1} , which corresponds to the intercalation of K^+ into graphene to form KC_8 [29-32]. The low capacity of the pristine graphene is attributed to a high K^+ diffusion barrier in the narrow space of the interlayer of graphene, especially the graphene with multiple layers. The previous report revealed that expanding the interlayer of the graphene via modification of Fe_2O_3 significantly improved the capacity of graphene [33], which suggests that the appropriate modified graphene-based composites will possess better potassium storage performance.

In this work, the sandwich-like structured TiO_2 /graphene composite was prepared by a facile hydrothermal reaction combined with the following high-temperature calcination in argon atmosphere. When the resulted TiO_2 /graphene composite was used as an anode material for PIBs, it can exhibit the improved electrochemical performance. This composite has large charge capacity of 336.8 mAh g^{-1} at 100 mA g^{-1} and better cyclability and rate capability.

2. EXPERIMENTAL

2.1. synthesis of TiO_2 /graphene, graphene and TiO_2

According to our previous report [34], the graphene oxide (GO) powder was prepared using improved Hummers method. The GO powder (0.2 g) was thoroughly mixed with 0.8 g of NaOH, then $50.2 \mu\text{L}$ of butyl titanate was added dropwise to the above solution with strong stirring for 2 h, subsequently the resulted solution was poured into the autoclave with capacity of 100 mL. The autoclave was heated at $180 \text{ }^\circ\text{C}$ for 24 h, then naturally cooled to room temperature, and the precipitate was obtained by filtering and washing the autoclaved solution three times with distilled water. Afterwards, the precipitate was dried in vacuum freeze-dryer at $-56 \text{ }^\circ\text{C}$ for 72 h, heated to $350 \text{ }^\circ\text{C}$ and kept for 6 h, and then heated to $850 \text{ }^\circ\text{C}$ and held for 6 h in argon stream at a ramp rate of $5 \text{ }^\circ\text{C min}^{-1}$ to acquire TiO_2 /graphene composite. The control graphene was prepared by the similar synthesis procedure except without butyl titanate and NaOH. The control TiO_2 was also synthesized by the similar preparation process except without GO.

2.2. Physical and electrochemical characterizations

The phases of the prepared material were determined by X-ray diffractometer (XRD, PANalytical, X'Pert3 powder) using Cu-K α radiation at a scan rate of 2° min⁻¹. The morphology of as-prepared samples was investigated by scanning electron microscopy (SEM, HITACHI, SU5000) and transmission electron microscopy (TEM, JEOL, JEM-2100F). To determine the specific surface area of graphene and TiO₂/graphene, the N₂ adsorption/desorption measurement was carried out by a Nova Station B (Quanta Chrome), and the pore diameter and specific surface area of the samples were calculated using the Brunauer-Emmett-Teller (BET) and Barrett-Joyner-Halenda (BJH) methods, respectively. The Raman spectroscopic investigation of samples was also conducted by Renishaw 1000 spectrometer with excitation source of 780 nm and the Raman shift varies from 200 to 2500 cm⁻¹. The content of TiO₂ in TiO₂/graphene composite was estimated by thermogravimeter in air.

The electrochemical measurements were performed on 2016 type coin cells assembled in an argon-filled glove box. The counter electrode is potassium metal foil, and the electrolyte is 0.8 M KPF₆ in EC/DMC (1:1 by volume). The counter and working electrodes are separated by glass fiber (Whatman GF/D). The dried working electrodes consist of electroactive material, acetylene black and polyvinylidene fluoride with a weight ratio of 80:10:10. The discharge/charge tests were performed in a constant-current model between 0.01 and 3.0 V (vs. K⁺/K) at room temperature, the corresponding specific capacity of samples is computed on the total weight of graphene or TiO₂/graphene composite. A CHI660E electrochemical workstation was used to perform cyclic voltammetry on electrodes between potentials of 0.01 and 3.0 V (vs. K⁺/K).

3. RESULTS AND DISCUSSION

The XRD patterns of the prepared graphene and TiO₂/graphene composites are shown in Fig. 1a. A broad diffraction peak of the prepared graphene is clearly observed at around $2\theta=26.2^\circ$, matching with 0.34 nm for the interplanar spacing, which is the characteristic diffraction of plane (002) of graphene [35, 36]. The broad diffraction peak implies that the graphene is not a monolayered graphene and the graphene sheets may stack into multilayers. All the diffractions of TiO₂/graphene composites except the undefined diffraction peak located at $2\theta=25.9^\circ$ are in compliance with XRD pattern of the standard TiO₂ (PDF: 21-1272), and the sharp peaks indicate that TiO₂ of the TiO₂/graphene composite possesses the good crystallinity. This undefined diffraction peak may be caused by the diffractions overlap of graphene and TiO₂ peaks, and the shift for diffraction peak of the plane (002) of graphene to lower angle, which may result from the possible fact that some TiO₂ particles are embedded into the layer of graphene and enlarge the distance of interlayers of graphene. Meanwhile, the broad peak of graphene and TiO₂/graphene composite is observed at $2\theta=26.2^\circ$ and $2\theta=25.9^\circ$, respectively, according to Bragg equation ($2d\sin\theta=n\lambda$). The result shows that the interlayer spacing of graphene and TiO₂/graphene is 0.339 and 0.344 nm, respectively, hence, the interlayer spacing is expanded by 0.005 nm. The TiO₂ content of TiO₂/graphene composite measured by TG analysis is about 44.1 wt%, which is derived from the analysis of Fig. s1.

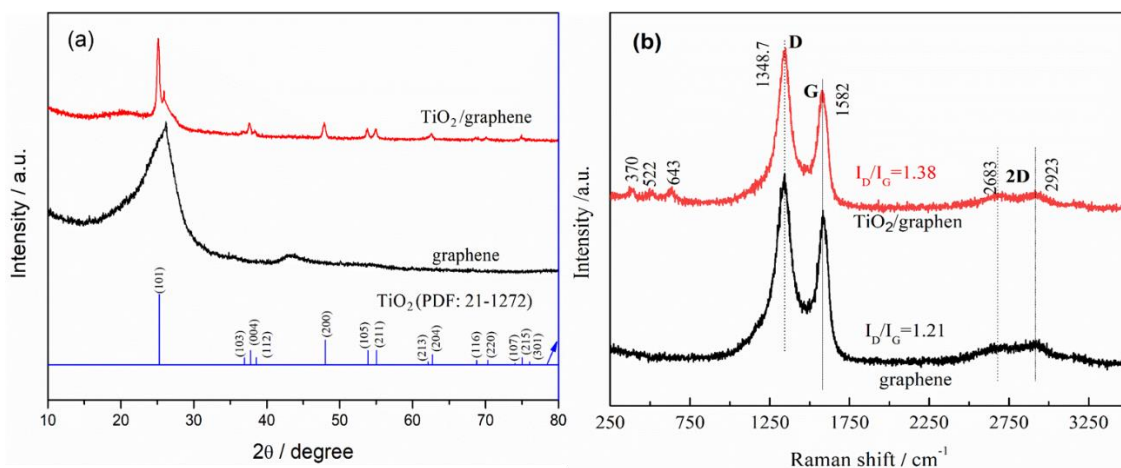


Figure 1. XRD patterns (a) and Raman spectra (b) of graphene and TiO₂/graphene.

To gain a deeper understanding of structural properties of the prepared materials, graphene and TiO₂/graphene were measured by Raman spectroscopy. Fig.1b presents Raman spectra of graphene and TiO₂/graphene and both two materials exhibit two strong peaks at about 1577.4 and 1348 cm⁻¹, which are attributed to characteristic Raman shift of the G and D bands of graphene [37, 38], respectively. The D band relates to disordered or defective carbon, while the G band is associated to graphitic sp² carbon.

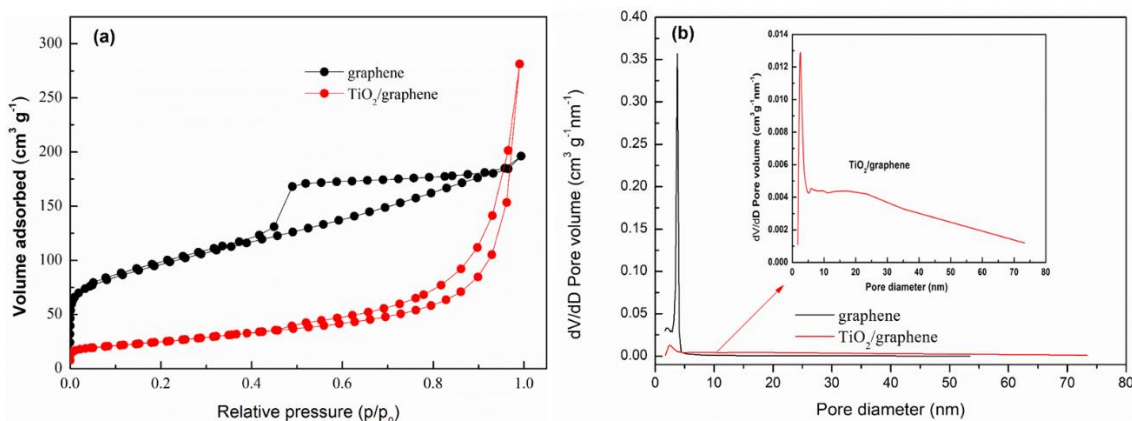


Figure 2. The N₂ adsorption-desorption isotherms (a), pore size distribution (b) of graphene and TiO₂/graphene. The inset of (b) illustrates the enlarged plot of pore size distribution of TiO₂/graphene.

The improved peak intensity ratio of D to G bands (I_D/I_G) of TiO₂/graphene (1.32) compared to that of graphene (1.21) demonstrates that the disorder and defect of graphene enhance after introduction of TiO₂. While the appearance of 2D bands in Raman spectra of both two samples implies that the number of layers decrease as compared to the exfoliated graphene. Additionally, the TiO₂/graphene shows the broad and low intensity peaks at 370, 522 and 643 cm⁻¹, corresponding to the characteristic Raman shift of TiO₂ [39-42], suggesting that some TiO₂ nanoparticles are not coated by graphene or do not embed into the interlayer of graphene.

To compare the specific surface area of the two prepared materials, N₂ adsorption/desorption method was used to determine surface area of graphene and TiO₂/graphene, and the corresponding adsorption/desorption isotherms are depicted in Fig.2a. As illustrated in Fig.2a, both graphene and TiO₂/graphene exhibit distinctive type-IV isotherms, demonstrating that both graphene and TiO₂/graphene are mesoporous. Based on Brunauer-Emmett-Teller method, the calculated surface area of graphene and TiO₂/graphene is 329.3 and 90.1 m²/g, respectively, implying that TiO₂ particles may embed into the pores or interlayers of graphene and hence the surface area of graphene decreases. As shown in Fig.2b, the pore size of both graphene and TiO₂/graphene is almost in the range of 2-50 nm, suggesting that both graphene and TiO₂/graphene are mesoporous, in accordance with the analysis of N₂ adsorption/desorption isotherms. The pore volume of graphene significantly decreases after introduction of TiO₂, hinting that some TiO₂ particles reside in the pores of graphene.

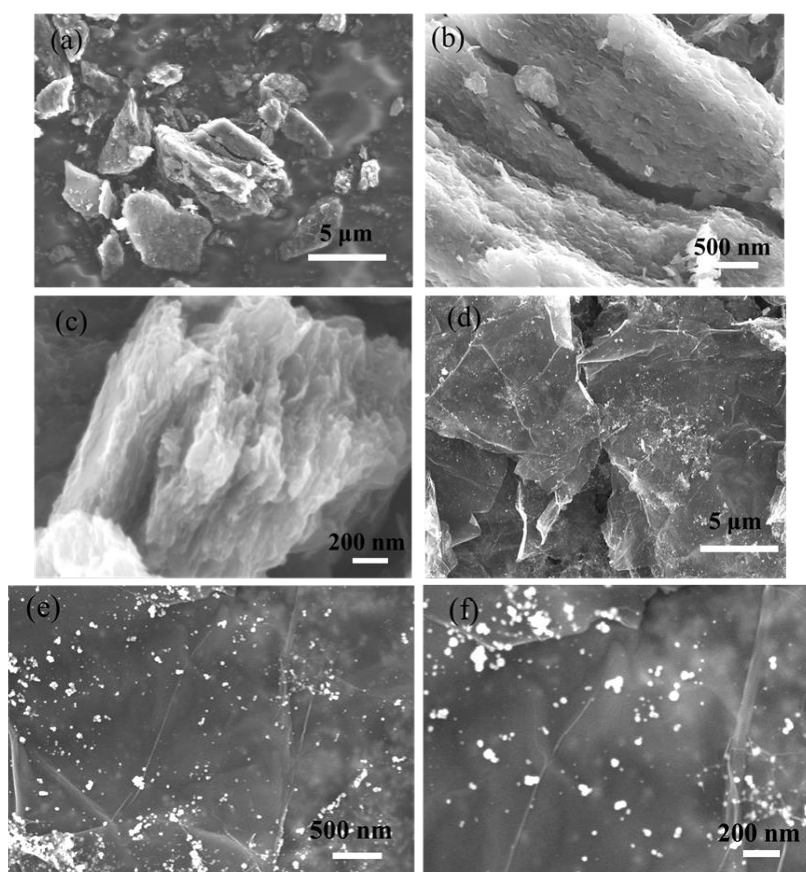


Figure 3. SEM images in different magnification of graphene (a-c) and TiO₂/graphene (d-f).

The SEM images of the two as-prepared materials are displayed in Fig.3. The graphene shows the laminated and porous microstructure stacked with graphene sheet by sheet, which is consistent with the high surface area of graphene. This special microstructure of graphene is beneficial for graphene to buffer the volume expansion upon charging, resulting in improved cycle performance of graphene. Unlike the graphene, the TiO₂/graphene composite is composed of sheets and particles. The SEM images of TiO₂/graphene composite in high magnification indicate that a majority of nanoparticles are

distributed in the interlayers of graphene and a minority of particles are attached to the surface of graphene. The distribution of nanoparticles in the interlayers of graphene is helpful to enlarge the space for the rapid infiltration of electrolyte. According to properties of graphene and the SEM images of graphene shown in Figs. 3a, 3b and 3c, the nanoparticles presented in Figs. 3d, 3e and 3f can be ascribed to TiO_2 .

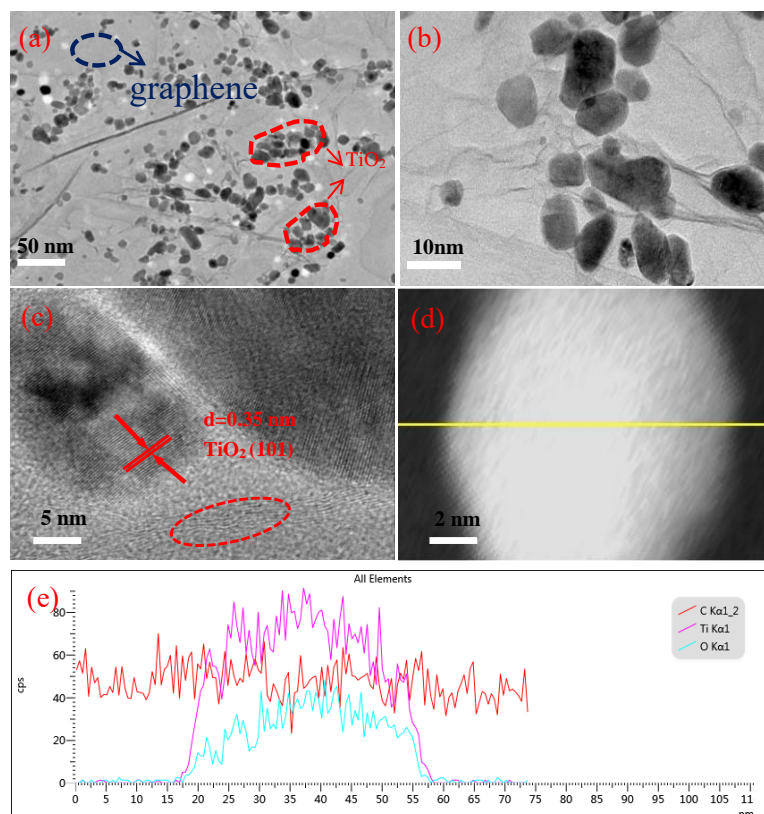


Figure 4. TEM images (a-b) and HRTEM images (c-d) of TiO_2 /graphene, compositional profiles (e) derived from the line-scanning analysis of (d).

The TEM and HRTEM were used to further learn the microstructure of TiO_2 /graphene and the corresponding images are depicted in Fig.4. Figs. 4a and 4b reveal that the TiO_2 particles are of size of 5-20 nm, some TiO_2 nanoparticles reside on the graphene sheet and some TiO_2 nanoparticles are embedded into the interlayers of graphene, which agrees with the SEM results of Figs. 3d, 3e and 3f. An interplanar spacing of 0.35 nm is observed in HRTEM image of TiO_2 /graphene (Fig.4c), and matches with the crystal plane (101) of TiO_2 . In addition, a distorted lattice fringe is clearly presented, which is similar to the reported graphene composite [43-45]. The TEM line-scanning analysis was employed to analyze the latitudinal element distribution of the nanoparticle shown in Fig.4d, and the results are depicted in Fig.4e, implying that the carbon content is almost unchanged with the measured distance. While the contents of both the Ti and O elements increase with the investigated distance from 0 to a constant value then decrease to 0, which may hint that TiO_2 nanoparticles are anchored on the surface of graphene or are coated by graphene.

The microstructure and compositional distribution were further studied by scanning transmission electron microscopy (STEM) coupled with energy dispersive X-ray spectroscopy (EDX) to confirm the composition of TiO₂/graphene. The STEM image (Fig.5a) demonstrates the lamellar microstructure with the evenly distributed nanoparticles of TiO₂/graphene, in consistence with the results of SEM and TEM. The EDX elemental mappings presented in Figs. 5b, 5c and 5d reveal the uniform distribution of C, Ti and O elements, suggesting that TiO₂ may be evenly dispersive in TiO₂/graphene. The compositional profiles (Fig.5e) verify that only elements C, Ti and O exist without any impurities in the prepared TiO₂/graphene composite. As observed in Fig.5f, the selected area electron diffraction patterns were indexed and corresponded to the planes (101), (112) and (200) of TiO₂, implying that TiO₂ is well-crystallized in the TiO₂/graphene, in agreement with the XRD result.

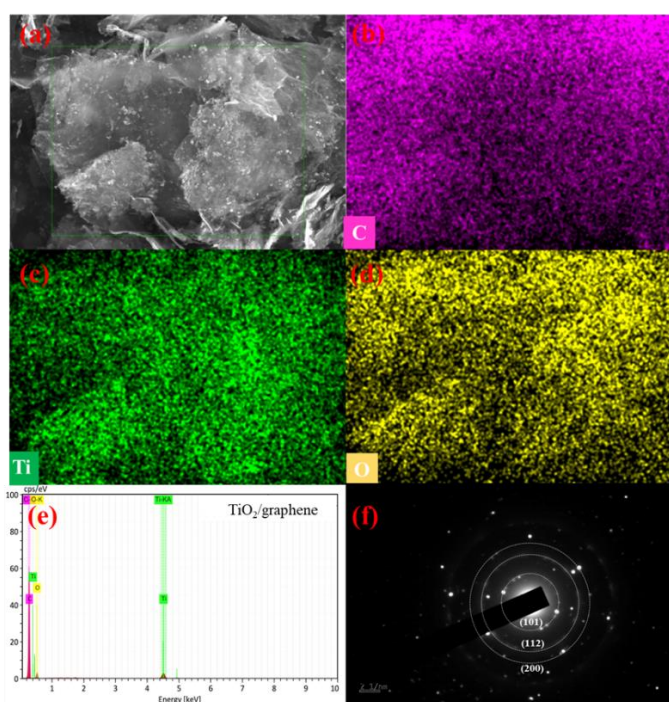


Figure 5. STEM image (a), EDX elemental mappings of C (b), Ti (c) and O (d), compositional profiles derived from EDX (e), SAED pattern (f) of TiO₂/graphene.

The electrochemical behavior of graphene and TiO₂/graphene was investigated by cyclic voltammetry and the cyclic voltammograms (CVs) were recorded between 0.01 and 3.0 V (vs K⁺/K) at a sweep rate of 0.1 mV s⁻¹, and the corresponding first two CVs are depicted in Fig.6. As observed in Fig.6a, graphene electrode exhibits a broad and well-defined anodic peak, a sharp cathodic peak and a small cathodic peak during the first cycle, resembling the previous graphene [27, 28]. During the cathodic process, K⁺ inserts into the graphene to construct potassiated graphene, electrolyte decomposes and solid electrolyte interface (SEI) forms on the surface of electroactive particles, while upon the anodic process, K⁺ is extracted from the potassiated graphene. Unlike the graphene, TiO₂/graphene electrode displays a broad but poorly defined anodic peak, possibly because graphene and TiO₂ anodic peaks

overlap. Compared with the cathodic curve of graphene, TiO₂/graphene does not show any additional peaks, which is linked with the electrochemical behavior of TiO₂ [46-48]. It is noted that the enclosed CV area of graphene electrode is bigger than that of TiO₂/graphene during the first cycle, suggesting that total capacity (the sum of charge and discharge capacities) of graphene is higher than that of TiO₂/graphene composite due to the proportionality between enclosed area and total capacity. However, the second cycle of CVs shown in Fig.6b demonstrates that TiO₂/graphene has a larger enclosed CV area than graphene, indicating that TiO₂/graphene exhibits higher total capacity than graphene during the second cycle. Additionally, Fig.6b shows a significant decrease in enclosed CV area between the first and second cycles, implying that capacity of both graphene and TiO₂/graphene dramatically decreases after the initial cycle. The absence of small reduction peak, which occurs at about 0.332 V during the first cycle, in Fig.6b indicates that stable SEI forms upon the second cycle. The anodic peak of the second cycle shifts to higher potential in comparison with that of the first cycle, which may result from the increase of the polarization when SEI forms and electrolyte decomposes.

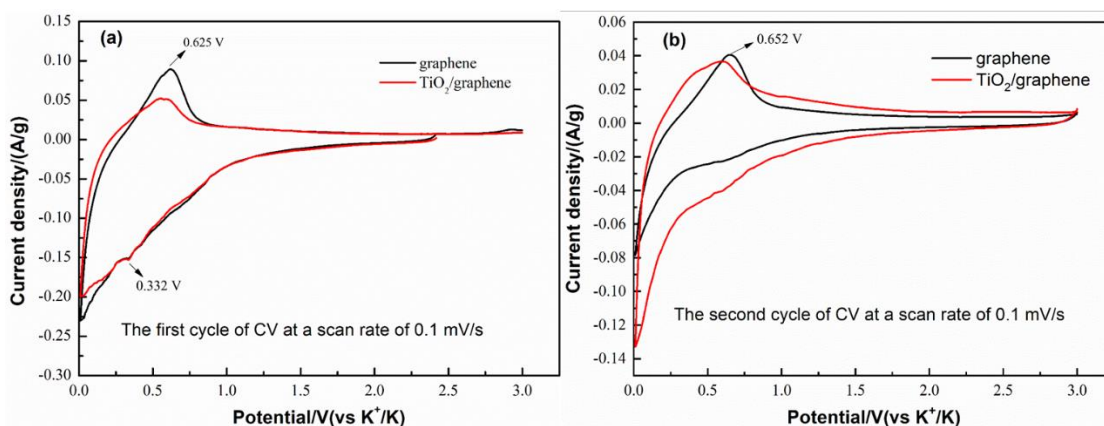


Figure 6. The first (a) and second (b) cycle CVs of graphene and TiO₂/graphene at a scan rate of 0.1 mV s⁻¹ in the potential range of 0.01-3.0 V (vs K⁺/K).

Fig.7 presents the discharge/charge profiles and cycle performance of graphene and TiO₂/graphene within the voltage range of 0.01-3.0 V (vs K⁺/K) at 100, 300 and 600 mA g⁻¹. The first two cycles of discharging/charging profiles of the two materials at 100, 300 and 600 mA g⁻¹ are depicted in Figs. 7a, 7b and 7c, respectively. It can be obviously seen that the capacity decreases with the current increase because the polarization becomes larger with current. The first discharge capacities of the both two electroactive materials at lower current densities significantly exceed the theoretical capacities of graphene and TiO₂, which is attributable to electrolyte decomposition and SEI formation. Additionally, discharge capacities of the second cycle dramatically fall in comparison with that of the first cycle, suggesting the great alleviation of the decomposition of electrolyte after the first cycle. As shown in Fig.7a, the initial charge capacity of graphene is 261.9 mAh g⁻¹ at 100 mA g⁻¹, and is almost equal to the theoretical capacity (279 mAh g⁻¹) of the pristine graphene, superior to that of about 200 mAh g⁻¹ of graphene [28] and N-doped graphene [27], and inferior to that of 290 mAh g⁻¹ of few-layer graphene

[31] and F-doped graphene [49]. When graphene is cycled at 100 mA g^{-1} , its initial discharge capacity is 950 mAh g^{-1} and the corresponding Coulombic efficiency is as low as 27.6%, and the such low Coulombic efficiency results from the electrolyte decomposition.

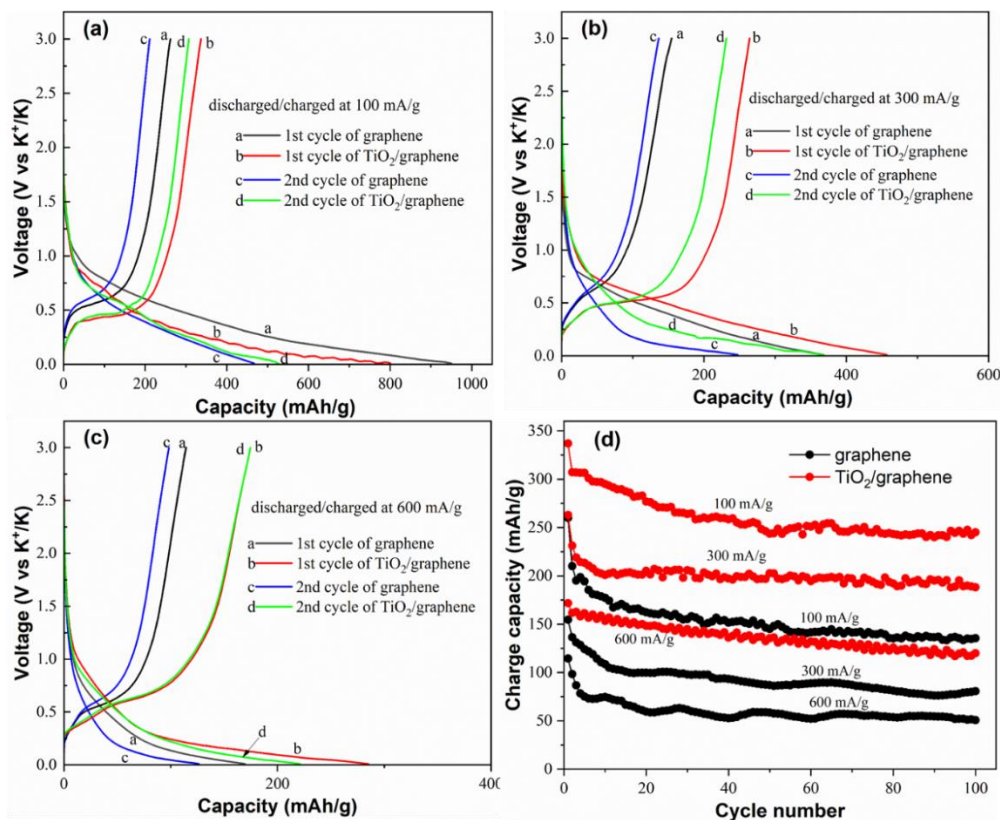


Figure 7. The first and second cycles of discharge/charge profiles of graphene and TiO₂/graphene at 100 mA g^{-1} (a), 300 mA g^{-1} (b) and 600 mA g^{-1} (c), and cycle performance of graphene and TiO₂/graphene (d).

Fig.7a also demonstrates that TiO₂/graphene exhibits the high charge capacity in the first cycle (336.8 mAh g^{-1}) and the second cycle (307 mAh g^{-1}) at 100 mA g^{-1} . The initial charge capacity of TiO₂/graphene is higher than that of graphene, the control TiO₂, FLG [27], TiO₂@NGC [46], Fe₂N@C [47], TiO₂/C nanofibers [48], TiO₂-RP/CN [48], SnS₂ [51], HeTiO₂eC [52] and MoO₂/C [53], and is somewhat lower than that of FLNG [31], FFGF [49] and SnS₂@rGO [54], as detailedly described in Table 1. The higher capacity of TiO₂/graphene may result from the synergetic effects of graphene and TiO₂. The discharge capacities of the first and second cycles of TiO₂/graphene at 100 mA g^{-1} are 800.5 and 528.7 mAh g^{-1} , respectively, and the corresponding Coulombic efficiencies are 42.1% and 58.1%, which are higher than that of graphene. The TiO₂/graphene presents the higher initial discharge capacity than graphene, resulting from the lower surface area of TiO₂/graphene in comparison with graphene.

Table 1. Comparison of the results in this work with some reported anode materials for PIBs.

Anode material	Initial charge capacity	Remaining capacity (mAh g ⁻¹)	Ref.
Few-layer graphene (FLG)	190 mAh g ⁻¹ at 100 mA g ⁻¹	150 (at 100 mA g ⁻¹) after 100 cycles	[27]
Few-layer nitrogen-doped graphene (FLNG)	352.2 mAh g ⁻¹ at 50 mA g ⁻¹	320 (at 50 mA g ⁻¹) after 60 cycles	[31]
TiO ₂ nanoparticle supported nitrogen-rich graphitic porous carbon (TiO ₂ @NGC)	228 mAh g ⁻¹ at 50 mA g ⁻¹	179 (at 50 mA g ⁻¹) after 100 cycles	[46]
Fe ₂ N@C	250 mAh g ⁻¹ at 100 mA g ⁻¹	150 (at 100 mA g ⁻¹) after 200 cycles	[47]
TiO ₂ /C nanofibers	179.8 mAh g ⁻¹ at 50 mA g ⁻¹	193.2 (at 50 mA g ⁻¹) after 500 cycles	[48]
Red phosphorus embedded in TiO ₂ /C nanofibers (TiO ₂ -RP/CN)	280.7 mAh g ⁻¹ at 50 mA g ⁻¹	257.8 (at 50 mA g ⁻¹) after 500 cycles	[48]
Few-layer F-Doped Graphene Foam (FFGF)	355.6 mAh g ⁻¹ at 50 mA g ⁻¹	165.9 (at 50 mA g ⁻¹) after 200 cycles	[49]
Flake-SnS ₂	328 mAh g ⁻¹ at 100 mA g ⁻¹	206 (at 100 mA g ⁻¹) after 30 cycles	[51]
hierarchical tubular TiO ₂ /carbon (HeTiO ₂ eC)	241 mAh g ⁻¹ at 100 mA g ⁻¹	197.5 (at 100 mA g ⁻¹) after 200 cycles	[52]
MoO ₂ /C	264 mAh g ⁻¹ at 100 mA g ⁻¹	155.2 (at 200 mA g ⁻¹) after 100 cycles	[53]
SnS ₂ @rGO	444.8 mAh g ⁻¹ at 50 mA g ⁻¹	387 (at 50 mA g ⁻¹) after 100 cycles	[54]
TiO ₂ /graphene	337 mAh g ⁻¹ at 100 mA g ⁻¹	245 (at 100 mA g ⁻¹) after 100 cycles	This work

As can be seen from Figs. 7b and 7c, the initial discharge capacity of graphene decreases to 364 and 169.7 mAh g⁻¹ with current density increasing to 300 and 600 mA g⁻¹, and the corresponding charge capacity falls to 154.6 and 114.4 mAh g⁻¹, matching with the low Coulombic efficiency of 42.5% and 67.4%, respectively. As for the second cycle of discharge/charge profiles of graphene, the discharge capacities of graphene decrease from 466.9 (100 mA g⁻¹) to 247.5 (300 mA g⁻¹) and 126.4 mAh g⁻¹ (600 mA g⁻¹), and the matching Coulombic efficiencies increase from 45.4% to 55.2% and 77.8%, respectively. Compared with the graphene, as depicted in Fig.s2a, the control TiO₂ exhibits much lower charge capacities of 31.1, 26.3 and 12.0 mAh g⁻¹ at 100, 300 and 600 mA g⁻¹, respectively, and the corresponding Coulombic efficiencies are 69.9%, 79.7% and 81.6%. The control TiO₂ has lower capacity than the previously reported TiO₂ (50 mAh g⁻¹) [50] and its capacity is significantly lower than 335.4 mAh g⁻¹ for the theoretical capacity of TiO₂, which is reckoned based on the assumption that one K⁺ intercalates into one TiO₂ formulae, and the low actual capacity is associated with the low electric conductivity of TiO₂.

Even though the capacity declines as the current density increases, the initial charge capacities of TiO₂/graphene at 300 and 600 mA g⁻¹ are still as high as 264 and 174.6 mAh g⁻¹, respectively, demonstrating that TiO₂/graphene is capable of the better rate capability. The second cycle capacity of TiO₂/graphene lessens as compared to the first cycle and the charge capacity difference between the first two cycles dwindles with the current density increasing. The negligible difference between the first and the second charge capacities at 600 mA g⁻¹ implies that TiO₂/graphene may possess the excellent cyclability at high current densities.

Fig.7d depicts the relationship between charge capacity of electroactive materials with varying current density and the cycle number. It is clearly seen that both graphene and TiO₂/graphene exhibit improved cycle performance with current density increasing. When cycled 100 times, graphene presents charge capacities of 135.5, 80.5 and 50.7 mAh g⁻¹ at 100, 300 and 600 mA g⁻¹, respectively. While

TiO₂/graphene keeps charge capacities of 245, 188.1 and 120 mAh g⁻¹ at 100, 300 and 600 mA g⁻¹, respectively, after 100 cycles. Compared with both graphene and TiO₂/graphene, the control TiO₂ presents humble cycle performance and capacity (Fig. s2b). The aforementioned results indicate that TiO₂/graphene possesses the improved capacity, cyclability and rate capability over the graphene and TiO₂. The improved electrochemical performance of TiO₂/graphene may result from the special sandwich-like microstructure of TiO₂/graphene composite that electroactive TiO₂ nanoparticles are embedded into the interlayer of mesoporous graphene. The nanosized graphene with mesopores facilitates the electrolyte penetration and the rapid diffusion of K⁺ in graphene, and the TiO₂ nanoparticles in the interlay of graphene can dampen volumetric expansion of the potassiated graphene, resulting in the better electrochemical performance of graphene. Furthermore, the highly intrinsic electrical conductivity of graphene is favorable to improve the potassium storage performance of TiO₂ nanoparticles. Hence, the synergetic effects of graphene and TiO₂ in TiO₂/graphene composite with sandwich-like microstructure may be accountable for the considerably enhanced electrochemical performance of TiO₂/graphene.

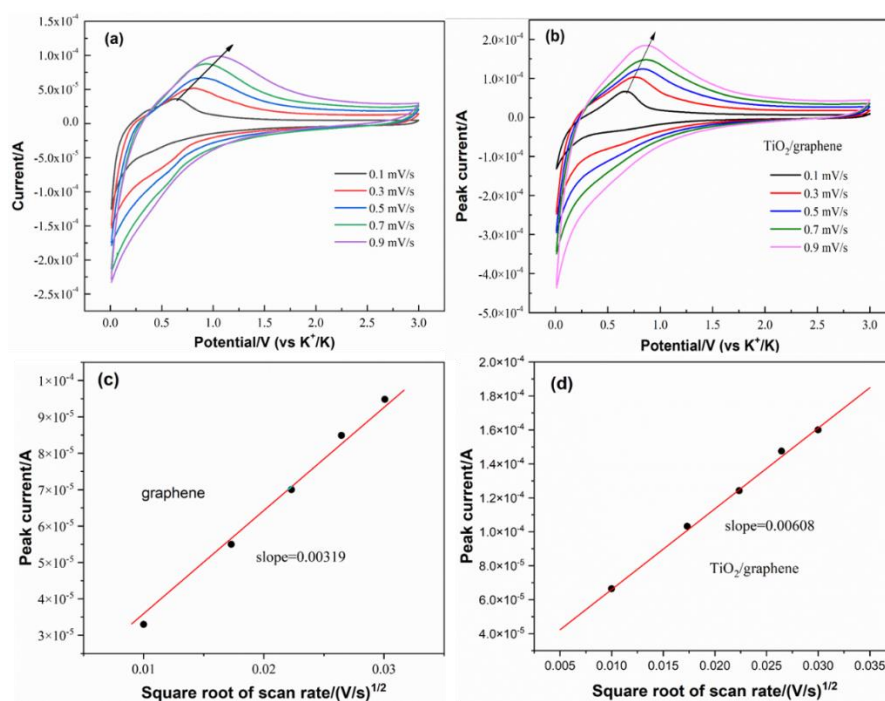


Figure 8. Cyclic voltammograms of graphene (a) and TiO₂/graphene (b) at various scan rates in the potential range of 0.01-3.0 V (vs. K^{+/K}), and relationship between current peak (*i_p*) and square root of scan rate (*v*^{1/2}) of graphene (c) and TiO₂/graphene (d) derived from (a) and (b), respectively.

To explain why TiO₂/graphene has better electrochemical performance than graphene, the comparisons of the diffusion coefficients of K⁺, *D_K*, in these two electrode materials are carried out because *D_K* is a key parameter to characterize the electrochemical kinetics of electroactive materials, and

the higher values of D_k suggest that the corresponding electroactive materials have better electrochemical performance. To obtain the D_k values of electroactive materials, electrode, which was galvanostatically discharged and charged four cycles, was tested by cyclic voltammetry at sweeping rates increasing from 0.1 to 0.9 mV s⁻¹ between potentials 0.01 and 3.0 V, and D_k is reckoned based on Eq.1, Randles–Sevick equation [55-57].

$$i_p = 2.69 \times 10^5 n^{3/2} A D_K^{1/2} C^0 \nu^{1/2} \quad (1)$$

In Eq.1, i_p is peak current (ampere) of CV, n stands for the number of exchanged electrons, A corresponds the area of electrode (cm²). C^0 is K⁺ concentration of the potassiated electroactive materials (mol cm⁻³), while ν indicates the potential sweep rate (V s⁻¹). The corresponding CVs of graphene and TiO₂/graphene are shown in Figs. 8a and 8b, respectively. As can be seen, the anodic peak shifts from lower potential to higher potential because polarization becomes larger as scan rate increases, but the cathodic peak potentials are almost unchanged. It is also observed that the anodic and cathodic peak currents increase with the scan rates increasing. Therefore, the simple comparison of D_k of graphene and TiO₂/graphene is calculated only based on anodic peak. In Figs.8c and 8d, peak current i_p is plotted against square root of sweep rate $\nu^{1/2}$ according to Figs. 8a and 8b, respectively. The linear correlations between i_p and $\nu^{1/2}$ reveal that diffusion of K⁺ in electroactive particles is a kinetically control step for the charge/discharge processes of both graphene and TiO₂/graphene [55, 58], and hence the computation of D_k of by graphene and TiO₂/graphene Eq.1 is reasonable. The figured D_k for graphene and TiO₂/graphene is 2.45×10^{-13} and 9.08×10^{-13} cm² s⁻¹, respectively, implying that TiO₂/graphene has faster kinetics of K⁺ diffusion in electroactive particles than graphene. The comparison of D_k for graphene and TiO₂/graphene successfully explains why TiO₂/graphene possesses superior electrochemical performance to graphene.

4. CONCLUSIONS

The TiO₂/graphene composite was synthesized by a facile hydrothermal reaction combined with a post high-temperature calcination under argon atmosphere, using GO, butyl titanate and NaOH as raw materials. The TiO₂/graphene composite possesses high surface area and the special microstructure that dispersive TiO₂ nanoparticles are attached to the surface and reside in the interlay of graphene nanosheets with mesopores. The special microstructure and the synergetic effects of graphene and TiO₂ endow the TiO₂/graphene composite with superior potassium storage performance to that of both graphene and TiO₂. This work highlights that the expanding interlayer distance of graphene by electroactive nanoparticles is an effective and facile strategy to upgrade the potassium storage performance of graphene-based composite anode materials for potassium-ion batteries.

SUPPLEMENTARY MATERIAL:

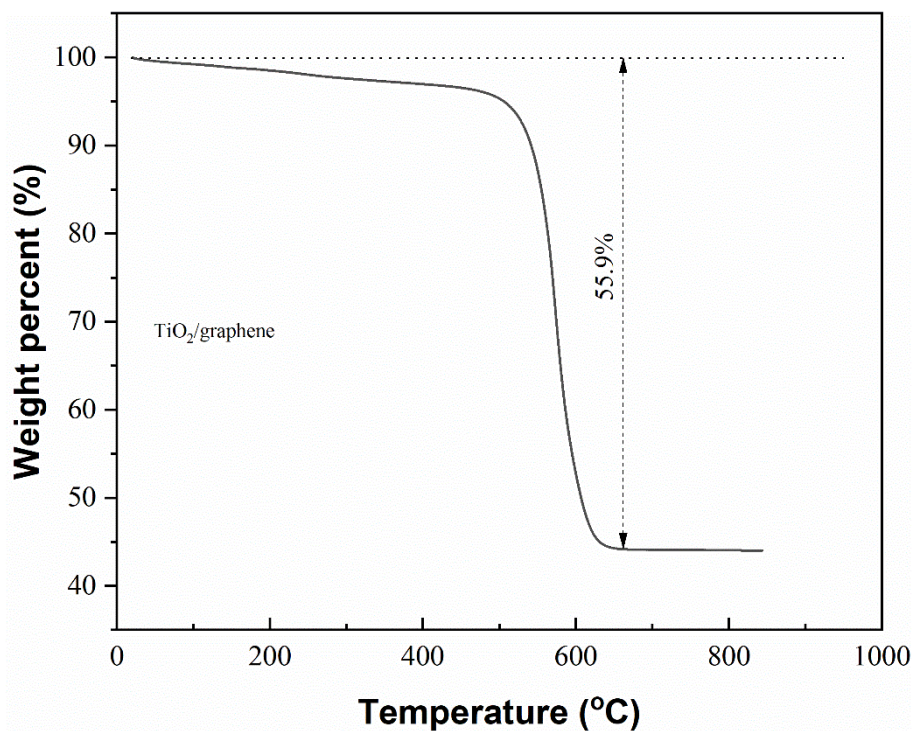
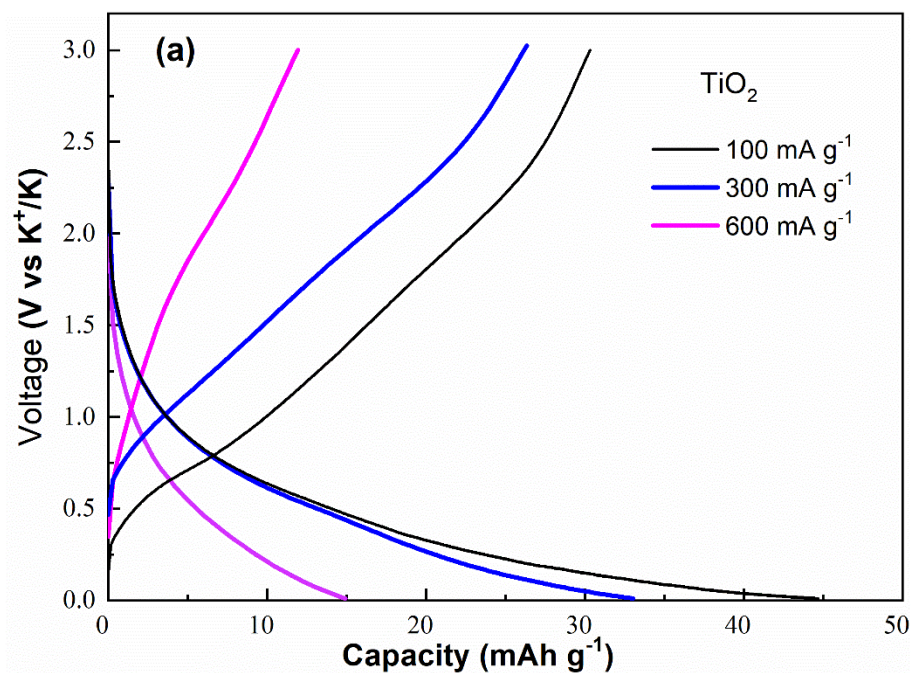


Fig.s1. Thermogravimetric curves of TiO₂/graphene composites in air from room temperature to 850 °C at a ramp rate of 5 °C/min.



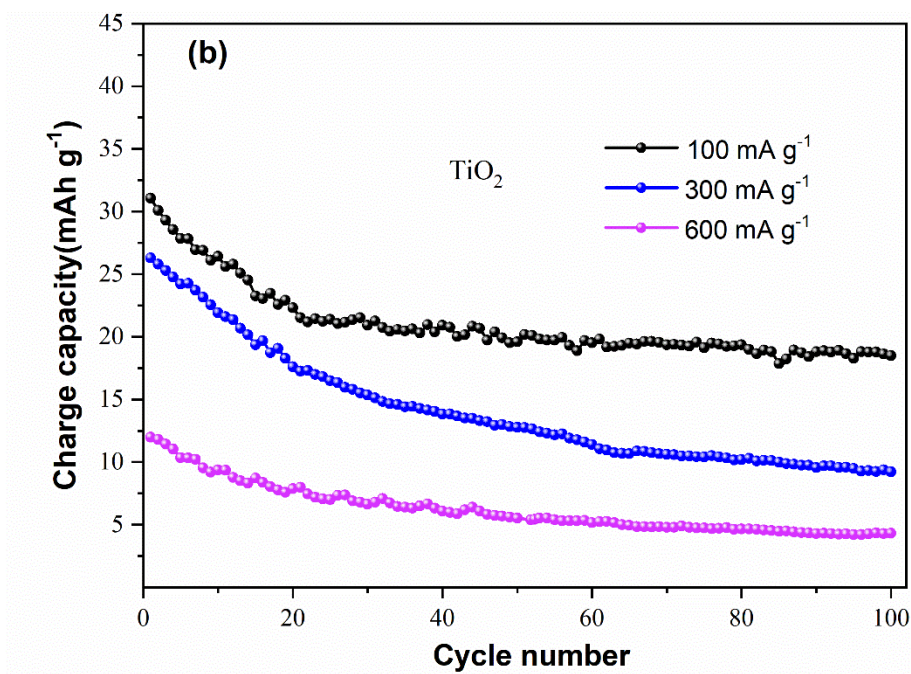


Fig.s2. The discharge/charge profiles (a) and cycle performance (b) of the control TiO₂ at various current densities.

ACKNOWLEDGEMENTS

The authors are grateful to the National Natural Science Foundation of China (No. 52164027), the Natural Science Foundation of Guangxi Province (No. 2021GXNSFAA220063), and research startup funds of Taizhou University for their financial assistance.

References

1. X. Wu, D.P. Leonard, X. Ji, *Chem Mater.*, 29 (2017) 5031.
2. J. Xiang, L. Yang, L. Yuan, K. Yuan, Y. Zhang, Y. Huang, J. Lin, F. Pan, Y. Huang, *Joule*, 3 (2019) 2334.
3. Y. Sui, J. Zhou, X. Wang, L. Wu, S. Zhong, Y. Li, *Mater. Today*, 42 (2021) 117.
4. L. Fan, R. Ma, Q. Zhang, X. Jia, B. Lu, *Angew. Chem. Int. Ed.*, 58 (2019) 10500.
5. A. Liu, L. Zhang, H. Li, Q. Ma, Q. Chen, R. Hua, Z. Fu, H. Kang, C. Zhang, H. Li, *J. Alloys Compd.*, 902 (2022) 163734.
6. F.J. Sonia, M.K. Jangid, M. Aslam, P. Johari, A. Mukhopadhyay, *ACS Nano*, 13 (2019) 2190.
7. W. Cao, E. Zhang, J. Wang, Z. Liu, J. Ge, X. Yu, H. Yang, B. Lu, *Electrochim. Acta*, 293 (2019) 364.
8. I. Sultana, T. Ramireddy, M.M. Rahman, Y. Chen, A.M. Glushenkov, *Chem. Commun.*, 52 (2016) 9279.
9. J. Huang, X. Lin, H. Tan, B. Zhang, *Adv. Energy Mater.*, 8 (2018) 1703496.
10. H. Ding, J. Wang, L. Fan, Z. Liu, X. Jia, X. Yu, B. Lu, *Chem. Eng. J.*, 395 (2020) 125147.
11. I. Sultana, M.M. Rahman, Y. Chen, A.M. Glushenkov, *Adv. Funct. Mater.*, 28 (2018) 1703857.
12. J. Han, M. Xu, Y. Niu, G.-N. Li, M. Wang, Y. Zhang, M. Jia, C.M. Li, *Chem. Commun.*, 52 (2016) 11274.
13. B. Kishore, G. Venkatesh, N. Munichandraiah, *J. Electrochem. Soc.*, 163 (2016) A2551.

14. L. Xu, Y. Wang, C. Lin, X. Xia, X. Chen, P. Xiong, Q. Chen, M. Wei, Q. Qian, L. Zeng, *J. Alloys Compd.*, 892 (2022) 162177.
15. L. Ma, Y. Lv, J. Wu, C. Xia, Q. Kang, Y. Zhang, H. Liang, Z. Jin, *Nano Res.*, 14 (2021) 4442.
16. D. Su, Y. Pei, L. Liu, Z. Liu, J. Liu, M. Yang, J. Wen, J. Dai, H. Deng, G. Cao, *Nano-Micro Lett.*, 13 (2021) 107.
17. J. Ge, L. Fan, J. Wang, Q. Zhang, Z. Liu, E. Zhang, Q. Liu, X. Yu, B. Lu, *Adv. Energy Mater.*, 8 (2018) 1801477.
18. Q. Liu, L. Fan, S. Chen, S. Su, R. Ma, X. Han, B. Lu, *Energy Technol.*, 7 (2019) 1900634.
19. Z. Jian, W. Luo, X. Ji, *J. Am. Chem. Soc.*, 137 (2015) 11566.
20. Z. Jian, Z. Xing, C. Bommier, Z. Li, X. Ji, *Adv. Energy Mater.*, 6 (2016) 150184.
21. Z. Jian, S. Hwang, Z. Li, A.S. Hernandez, X. Wang, Z. Xing, D. Su, X. Ji, *Adv. Funct. Mater.*, 27 (2017) 1700324.
22. Y. Xie, Y. Chen, L. Liu, P. Tao, M. Fan, N. Xu, X. Shen, C. Yan, *Adv. Mater.*, 29 (2017) 1702268.
23. X. Zhao, P. Xiong, J. Meng, Y. Liang, J. Wang, Y. Xu, *J. Mater. Chem. A*, 5 (2017) 19237.
24. L. Wang, J. Yang, J. Li, T. Chen, S. Chen, Z. Wu, J. Qiu, B. Wang, P. Gao, X. Niu, H. Li, *J. Power Sources*, 409 (2019) 24.
25. X. Wu, Y. Chen, Z. Xing, C.W.K. Lam, S.-S. Pang, W. Zhang, Z. Ju, *Adv. Energy Mater.*, 9 (2019) 1900343.
26. G. Wang, M. Yu, X. Feng, *Chem. Soc. Rev.*, 50 (2021) 2388.
27. K. Share, A.P. Cohn, R. Carter, B. Rogers, C.L. Pint, *ACS Nano*, 10 (2016) 9738.
28. K. Share, A.P. Cohn, R.E. Carter, C.L. Pint, *Nanoscale*, 8 (2016) 16435.
29. S. Gong, Q. Wang, *J. Phys. Chem. C*, 121 (2017) 24418.
30. G. Ma, K. Huang, J.-S. Ma, Z. Ju, Z. Xing, Q.-c. Zhuang, *J. Mater. Chem. A*, 5 (2017) 7854.
31. Z. Ju, P. Li, G. Ma, Z. Xing, Q. Zhuang, Y. Qian, *Energy Storage Mater.*, 11 (2018) 38.
32. J. Li, W. Qin, J. Xie, H. Lei, Y. Zhu, W. Huang, X. Xu, Z. Zhao, W. Mai, *Nano Energy*, 53 (2018) 415.
33. X. Qiao, C. Niu, D. Liao, Z. Chen, L. Sun, Y. Xu, *Adv. Funct. Mater.*, 31 (2021) 2105145.
34. L. Hu, S. Zheng, Z. Chen, B. Huang, J. Yang, Q. Chen, *Electrochim. Acta*, 284 (2018) 609.
35. Y. Wang, S. Gao, X. Zang, J. Li, J. Ma, *Anal. Chim. Acta*, 716 (2012) 112.
36. V.S. Kindalkar, K. K. S. Bhat, S.M. Dharmaprakash, *Mater. Chem. Phys.*, 261 (2021) 124224.
37. G. Wang, J. Yang, J. Park, X. Gou, B. Wang, H. Liu, J. Yao, *J. Phys. Chem. C*, 112 (2008) 8192.
38. G. Wang, X. Shen, J. Yao, J. Park, *Carbon*, 47 (2009) 2049.
39. H.C. Choi, Y.M. Jung, S.B. Kim, *Vib. Spectrosc.*, 37 (2005) 33.
40. H.Y. Wang, X.J. Xu, J.H. Wei, R. Xiong, J. Shi, *Solid State Phenom.*, 181-182 (2012) 422.
41. M.C. Mathpal, A.K. Tripathi, M.K. Singh, S.P. Gairola, S.N. Pandey, A. Agarwal, *Chem. Phys. Lett.*, 555 (2013) 182.
42. K.Y. Kumar, H. Saini, D. Pandiarajan, M.K. Prashanth, L. Parashuram, M.S. Raghu, *Catal. Today*, 340 (2020) 170.
43. B. Zhang, M. Cheng, G. Liu, Y. Gao, L. Zhao, S. Li, Y. Wang, F. Liu, X. Liang, T. Zhang, G. Lu, *Sens. Actuators B Chem.*, 263 (2018) 387.
44. H. Wang, J. Chen, P. Wang, C. Liang, K. Yu, *J. Alloys Compd.*, 918 (2022) 165785.
45. Y. Wang, M. Li, P. Peng, H. Gao, J. Wang, B. Sun, *J. Alloys Compd.*, 900 (2022) 163304.
46. D.P. Dubal, A. Schneemann, V. Ranc, Š. Kment, O. Tomanec, M. Petr, H. Kmentova, M. Otyepka, R. Zbořil, R.A. Fischer, K. Jayaramulu, *Adv. Energy Sus. Res.*, 2 (2021) 2100042.
47. Y. Du, W. Weng, Z. Zhang, Y. He, J. Xu, T. Yang, J. Bao, X. Zhou, *Chinese J. Chem.*, 39 (2021) 1878.
48. D. Su, J. Dai, M. Yang, J. Wen, J. Yang, W. Liu, H. Hu, L. Liu, Y. Feng, *Nanoscale*, 13 (2021) 6635.
49. Z. Ju, S. Zhang, Z. Xing, Q. Zhuang, Y. Qiang, Y. Qian, *ACS Appl. Mater. Inter.*, 8 (2016) 20682.
50. K.G. Reeves, J. Ma, M. Fukunishi, M. Salanne, S. Komaba, D. Dambournet, *ACS Appl. Energy*

Mater., 1 (2018) 2078.

51. H. Rong, Y. Z. Fang, X. Y. Liu, K. Zhu, D. X. Cao, Y. I. Jin, G. L. Wang, *Chem. Res. Chinese Universities*, 37 (2021) 311.
52. Y. Li, C. Yang, F. Zheng, Q. Pan, Y. Liu, G. Wang, T. Liu, J. Hu, M. Liu, *D Nano Energy*, 59(2019) 582.
53. L.M. Chen, B.Huang, J.W. Yang, Y.W. Li, Q.Q. Chen, S.H. Xiao, W. Li, *Int. J. Electrochem. Sci.*, 16 (2021) 211216
54. L. Fang, J. Xu, S. Sun, B. Lin, Q. Guo, D. Luo, H. Xia, *Small*, 15(2019) 1804806.
55. A.J. Bard, L.R. Faulkner, J. Leddy, C.G. Zoski, *Electrochemical methods: fundamentals and applications*, JOHN WILEY & SONS, INC.(1980) New York, United States of America.
56. Q. Zhu, S. Zheng, X. Lu, Y. Wan, Q. Chen, J. Yang, L.-z. Zhang, Z. Lu, *J. Alloys Compd.*, 654 (2016) 384.
57. S. Zheng, S. Cheng, S. Xiao, L. Hu, Z. Chen, B. Huang, Q. Liu, J. Yang, Q. Chen, *J. Alloys Compd.*, 815 (2020) 152379.
58. H. Lindström, S. Södergren, A. Solbrand, H. Rensmo, J. Hjelm, A. Hagfeldt, S.-E. Lindquist, *J. Phys. Chem. B*, 101 (1997) 7717.

© 2022 The Authors. Published by ESG (www.electrochemsci.org). This article is an open access article distributed under the terms and conditions of the Creative Commons Attribution license (<http://creativecommons.org/licenses/by/4.0/>).